

# Fast and Deterministic Fabrication of Sub-5 Nanometer Solid-State Pores by Feedback-Controlled Laser Processing

Ernan Zvuloni, Adam Zreben, Tal Gilboa, and Amit Meller\*



Cite This: <https://doi.org/10.1021/acsnano.1c03773>



Read Online

ACCESS |



Metrics & More



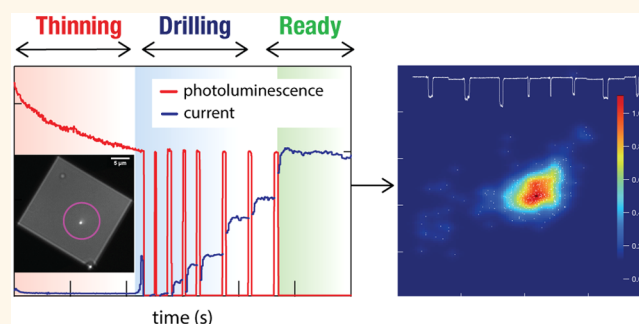
Article Recommendations



Supporting Information

**ABSTRACT:** Nanopores are single-molecule sensors capable of detecting and quantifying a broad range of unlabeled biomolecules including DNA and proteins. Nanopores' generic sensing principle has permitted the development of a vast range of biomolecular applications in genomics and proteomics, including single-molecule DNA sequencing and protein fingerprinting. Owing to their superior mechanical and electrical stability, many of the recent studies involved synthetic nanopores fabricated in thin solid-state membranes such as freestanding silicon nitride. However, to date, one of the bottlenecks in this field is the availability of a fast, reliable, and deterministic fabrication method capable of repeatedly forming small nanopores (i.e., sub 5 nm) *in situ*. Recently, it was demonstrated that a tightly focused laser beam can induce controlled etching of silicon nitride membranes suspended in buffered aqueous solutions. Herein, we demonstrate that nanopore laser drilling (LD) can produce nanopores deterministically to a prespecified size without user intervention. By optimizing the optical apparatus, and by designing a multistep control algorithm for the LD process, we demonstrate a fully automatic fabrication method for any user-defined nanopore size within minutes. The LD process results in a double bowl-shaped structure having a typical size of the laser point-spread function (PSF) at its openings. Numerical simulations of the characteristic LD nanopore shape provide conductance curves that fit the experimental result and support the idea that the pore is produced at the thinnest area formed by the back-to-back facings bowls. The presented LD fabrication method significantly enhances nanopore fabrication throughput and accuracy and hence can be adopted for a large range of biomolecular sensing applications.

**KEYWORDS:** solid-state nanopores, single-molecule sensing, photochemical etching, photoluminescence, laser drilling



Nanopores have emerged as highly versatile single-molecule sensors that can be adapted for a broad range of biological applications, including genomics, epi-genomics, transcriptomics, and proteomics.<sup>1,2</sup> To date, a variety of nanopore sensors have been developed, such as protein nanopores, glass nanocapillaries, and solid-state nanopores (ssNPs).<sup>2–5</sup> Regardless of the specific nanopore class, they share the same generic sensing principle: The nanopore is embedded or fabricated in an electrically insulating substrate, which divides the space into two small liquid reservoirs filled with an electrolyte solution. Since the nanopore serves as the only liquid connection between the two chambers, when an external electric potential is applied across it, a steady ionic flow occurs through the nanopore, called the open-pore current ( $i_0$ ).<sup>6</sup> The convergence of the ion's flow lines in the nanopore's vicinity creates a strong electric field gradient that attracts and focuses charged

biomolecules toward and through the nanopore.<sup>7</sup> As the molecules are entering the pore, they partially block the ion current allowing real-time sensing of biomolecules from a dilute solution by simply monitoring the time-dependent ion flow.

One of the most remarkable features of nanopores is their ability to sense unlabeled biomolecules in solution. Much like classical gel electrophoresis, which has been extensively used to sense multiple kinds of biomolecules in bulk, nanopores have

Received: May 4, 2021

Accepted: June 28, 2021

been adapted for basic life sciences applications ranging from DNA sequencing to characterization of DNA/protein interactions and detection of free proteins in solution.<sup>8</sup> Notably, recent studies even demonstrated ways for using nanopores with clinical samples including monitoring biomarkers in biofluids, such as plasma and saliva.<sup>9–14</sup> Moreover, nanopores have been suggested as key tools in futuristic applications such as DNA-based information storage.<sup>15–17</sup> Among the various nanopore types, planar ssNPs have been widely adapted for various sensing goals, due to their mechanical robustness, the ability to functionalize their surfaces using organic or inorganic treatments,<sup>18</sup> and the fact that they can be conveniently integrated in microfluidic devices used for upstream sample processing.<sup>19</sup> The possibility of complementing the purely electrical single-molecule sensing with opto-electrical modalities has further extended the scope of ssNP-based sensing.<sup>20–22</sup> Overall, these developments have created a growing unmet need for the development of highly robust, affordable, and deterministic ssNP fabrication techniques with specific molecular dimensions of a few nanometers.

To date, the fabrication of ssNPs in thin membranes has been accomplished by several approaches. One common method used a tightly focused beam of ions (e.g., Ga<sup>+</sup>)<sup>23,24</sup> in a Focused Ion Beam (FIB) apparatus or electrons in a field-emission Transmission Electron Microscope (TEM).<sup>25,26</sup> The energetic particles were shown to be able to blast atoms from the membrane, ultimately creating a nanopore at the desired point of impact. This approach is considered highly controllable, yet to date has remained manual and involves a dedicated trained user. Moreover, high-resolution TEM instruments are expensive and are not designed for high fabrication throughput. More recently, nanopore formation has been achieved by inducing stochastic dielectric breakdown (DB) at defect sites in the membrane, followed by enlargement of the pore with a series of high-amplitude electric pulses.<sup>27–29</sup> In contrast to the TEM approach, the DB-based drilling method is considered to be low-cost and accessible, and has the advantage of producing ssNPs in the aqueous environment. However, as DB relies on the breakdown and expansion of random defects in the membrane, it may involve large variability in ssNP 3D shape, drilling time, and pore location.<sup>29</sup>

One alternative to the current ssNPs drilling techniques is a laser-based approach for *in situ* ssNP fabrication using photochemical induced etching.<sup>30</sup> It was found that when the laser's photon energy is comparable to or larger than the material's electronic bandgap, a relatively low-power focused laser beam may induce rapid photochemical etching of free-standing SiN<sub>x</sub> membranes in an aqueous environment. Specifically, at alkaline conditions (pH 10), 50-nm-thick Si-rich SiN<sub>x</sub> membranes could be drilled in a few minutes using a <10 mW blue laser beam.<sup>31</sup> This discovery enables the development of a robust, rapid, and most importantly deterministic ssNP fabrication technique for molecular size nanopores. To advance laser-based ssNP drilling, increase its robustness, and ensure a highly deterministic fabrication, several obstacles must be addressed. One challenge is to determine the conditions that provide the greatest control over the rate and extent of each of the fabrication steps (membrane thinning, nanopore formation, and nanopore expansion). Having these conditions at hand, one can proceed to develop and validate a computer-controlled strategy to obtain an arbitrary ssNP size with high probability and within short processing time. Preferably, this approach would minimize or

eliminate user intervention in the processes, leading the way for high-throughput ssNP fabrication.

In this study, we present a subwavelength autofocusing optical design for drilling ssNPs, coupled to an end-to-end multistep algorithm for controlling the entire drilling process. Importantly, we achieved deterministic ssNP drilling with high accuracy and reproducibility. Specifically, our optimized system can complete the ssNP drilling within 2 min from beginning to end, with an error of less than 5% in the open-pore conductance corresponding to a sub-nanometer error in the pore dimensions. We numerically simulated the effect of the Gaussian form-factor of the laser-drilled pores on the electric field distribution and ionic current of the pores. Our results indicate that while the general Ohmic behavior remains similar to TEM-drilled nanopores, the distribution of the electrical field gradient near the pore favors molecule capture due to the wider-field distribution in the nanopore vicinity. The open-pore current calculated from the simulations was fitted to experimental data to obtain a more realistic approximation of ssNPs conductance dependence on pore diameter, as compared with the widely used theoretical model of ssNP conductance. We validated the functionality of the laser-drilled nanopore by performing translocations of denatured proteins immediately after drilling, such that the entire process of nanopore drilling and single-protein sensing took less than 20 min.

## RESULTS AND DISCUSSION

**Characterizing Laser Etching Kinetics of Nanoscale Apertures.** Before attempting to systematically manipulate and control the laser drilling (LD) process, we fabricated a custom sample that allows a thorough investigation of the laser-based etching kinetics. We hypothesized that as the full-width half-maximum (FWHM) of a tightly focused laser beam is much larger than the typical ssNP diameter, if the etching process is allowed to proceed freely it would result in the formation of an aperture having a size roughly of the beam's point spread function (PSF),  $\lambda/(2 \text{ NA})$ , where  $\lambda$  is the laser wavelength and NA is the objective's numerical aperture. However if the laser etching is timely terminated, it would permit the formation of ssNPs much smaller than the PSF size, and with fine control over the process kinetics, it can be used to create nanopores with nanometer resolution.

To image the etching process using TEM, we fabricated a two-layer model substrate consisting of a 50-nm-thick SiN<sub>x</sub> on which a 10 nm TiO<sub>2</sub> layer was deposited by atomic layer deposition (ALD). Previous studies revealed that the LD rate is extremely sensitive to the Si/N ratio in the free-standing SiN<sub>x</sub> film.<sup>31</sup> Specifically, nitride-rich membranes or stoichiometric Si<sub>3</sub>N<sub>4</sub> were found to remain nearly intact even when irradiation with high intensities of blue laser, whereas Si-rich membranes could be readily etched at relatively low laser intensities, even when exposed for brief lengths of time. This phenomenon is attributed to the smaller bandgap of the Si-rich membranes, which permits efficient electron excitation of the membrane by visible light. Consistent with this result, we find that free-standing, high-bandgap materials such as TiO<sub>2</sub> (3.0 eV for rutile and 3.2 eV for anatase)<sup>32,33</sup> remain intact even after extremely long (>300 s) and high-intensity (>30 mW) 488 nm laser irradiation focused to a diffraction-limited spot. Therefore, the TiO<sub>2</sub> layer deposited on top of a the SiN<sub>x</sub> membrane may provide a convenient means for analyzing the thinning progress using high-resolution TEM combined with

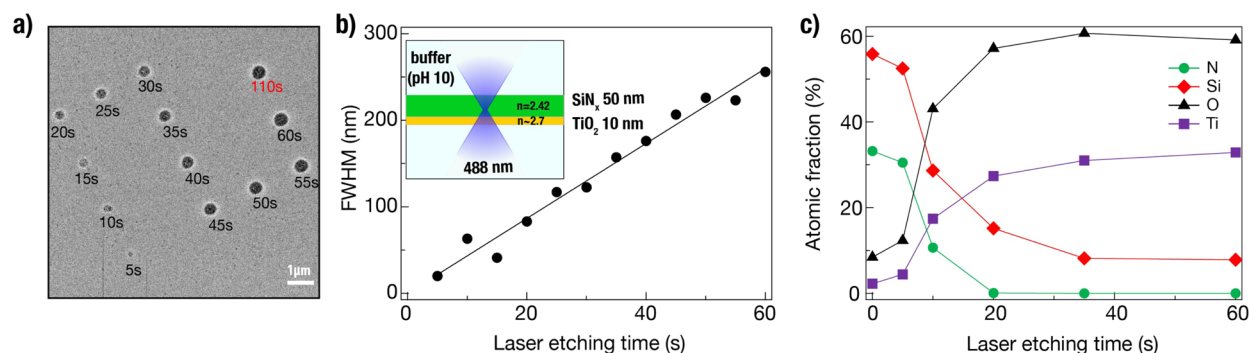


**Figure 1.** Characterization of the laser-drilling (LD) kinetics using transmission electron microscopy (TEM). (a) Left: A series of etch marks applied by the 488 nm laser at varying doses, imaged with TEM. The dose increases in 5 s increments from 5 to 60 s, with an additional overetching dose of 110 s. (b) Analysis of the FWHM obtained at different doses. The laser forms nanowells with a diameter that is linearly dependent on the laser dose. Inset: A schematic of the specimen used in this study. The 50 nm silicon nitride ( $\text{SiN}_x$ ) free-standing membrane was coated with a thin 10 nm layer of  $\text{TiO}_2$ , and the structure was etched by the Gaussian laser beam. (c) Elemental analysis by energy dispersive X-ray spectroscopy (EDS). The elemental compositions of the 5, 10, 20, 35, and 60 s etch marks were measured. The background was used for the 0 s point. The atomic fractions of the  $\text{TiO}_2$  elements increase, while the  $\text{SiN}_x$  elements decrease, demonstrating that LD depletes only specific elemental components of the membrane.

nanoscopic elemental analysis in which silicon, nitrogen, titanium, and oxygen are easily distinguished.

Figure 1a displays a TEM (FEI Titan Cubed Themis G2) image of the composite  $\text{SiN}_x/\text{TiO}_2$  50/10 nm membrane after illuminating the membrane with a focused 488 nm laser beam (18 mW measured before the objective lens; see Figure 2a) for variable doses from 5 to 60 s, as indicated. An additional dose ( $t = 110$  s) was performed as a long-time reference point, noting that longer exposures (roughly above 2 min) may not produce consistent results due to slow mechanical drift of the stage. We used high Si content ( $n = 2.42$ ) material deposited by low pressure chemical vapor deposition (LPCVD) and submerged in alkaline solution (pH 10) in this experiment. Based on previous studies,<sup>31</sup> these conditions are expected to result in nanopore formation in just a few seconds, should we use the bare  $\text{SiN}_x$  membrane. We find, however, that the 10 nm  $\text{TiO}_2$  layer prevents nanopore formation up to roughly 60 s of irradiation, while providing a strong contrast for imaging of the resulting nanowells using high resolution TEM. The FWHM of the nanowells as a function of the laser irradiation is shown in Figure 1b. Interestingly, and in accordance with previous reports, we see that laser etching can form sub-PSF-sized nanowells, with a diameter that is linearly dependent on the laser exposure time, ranging from about 20 to 250 nm. Moreover, a closer examination of the nanowell intensity suggests that for doses smaller than about 35 s, the intensity appears to be brighter than at later times. To further evaluate this finding, we performed energy dispersive X-ray spectroscopy (EDS) analysis of the nanowells by integrating the signal from a fixed area centered around each of the spots. As summarized in Figure 1c, Si and N atoms are depleted as time progresses, reaching a plateau at about 30 s. At the same time, and as expected, the content of Ti and O atoms rises in the first 30 s, reaching nearly 30% and 60%, respectively, for  $t > 30$  s.

The results shown in Figure 1 demonstrate that during the laser etching process, the  $\text{TiO}_2$  layer remained intact, while the Si and N atoms were evacuated to the surrounding hydroxyl-rich aqueous solution. Interestingly, the process kinetics indicate that even after a short exposure, the  $\text{TiO}_2$  layer becomes exposed with the formation of a sub-PSF nanowell: starting from a 5:1 ratio of  $\text{SiN}_x/\text{TiO}_2$  based on the initial layer thicknesses, one can see a steep inversion in the elemental

composition already at the 10 s time point. These results demonstrate the capability of a submicrometer optical beam to controllably form nanoscale wells. Evidently, a key to the process is maintaining the tightly and well-controlled laser focus at the membrane position and monitoring the process with a real-time algorithm. These are key features for the development of a deterministic LD method.

**Applying Real-Time Feedback Control for Deterministic LD of ssNPs.** To facilitate the optical feedback process and permit precise autofocusing, we designed an optomechanical system and developed a computer program to control the entire LD process, as shown schematically in Figure 2, panel a and panel b, respectively. The optical design includes a 405 nm CW laser coupled to a single-mode polarization preserving fiber. The single-mode fiber is used as a spatial filter ensuring a clean  $\text{TEM}_{00}$  mode, which is crucial for producing a diffraction-limited Gaussian laser spot. Before entering the microscope, the beam is expanded using a telescope made by two achromatic lenses forming an effective 5 $\times$  magnifying telescope, which ensures the microscope objective back-aperture is filled. The beam intensity is software-controlled by a variable intensity module and an on/off digital port switch for millisecond-scale intensity adjustment. This feature proved to be essential to the algorithm developed here, increasing its ability to deal with different membrane structures, thickness variations, etc. In this study, we used a 63 $\times$ /1.15 NA water immersion objective with a long working distance to permit focusing with minimal stress on the bottom cover slide. The sample is mounted on an XYZ piezo nanopositioner for accurate placement of the sample in front of the objective lens. The emitted light from the sample is filtered using a long-pass filter and is imaged using a scientific CMOS (sCMOS) camera. The camera is used to find and center the  $\text{SiN}_x$  window using white light illumination; to automatically focus the beam prior to drilling; and to measure photoluminescence (PL) during drilling. The sCMOS has a large dynamic range, which by using image processing allows one to compute the PL at various laser intensities. Accordingly, The PL is calculated by summing the 3-by-3 neighborhood of the brightest pixel in the frame.

We find that precise focusing of the beam at the membrane plane is critical for successful and reproducible LD. A slight

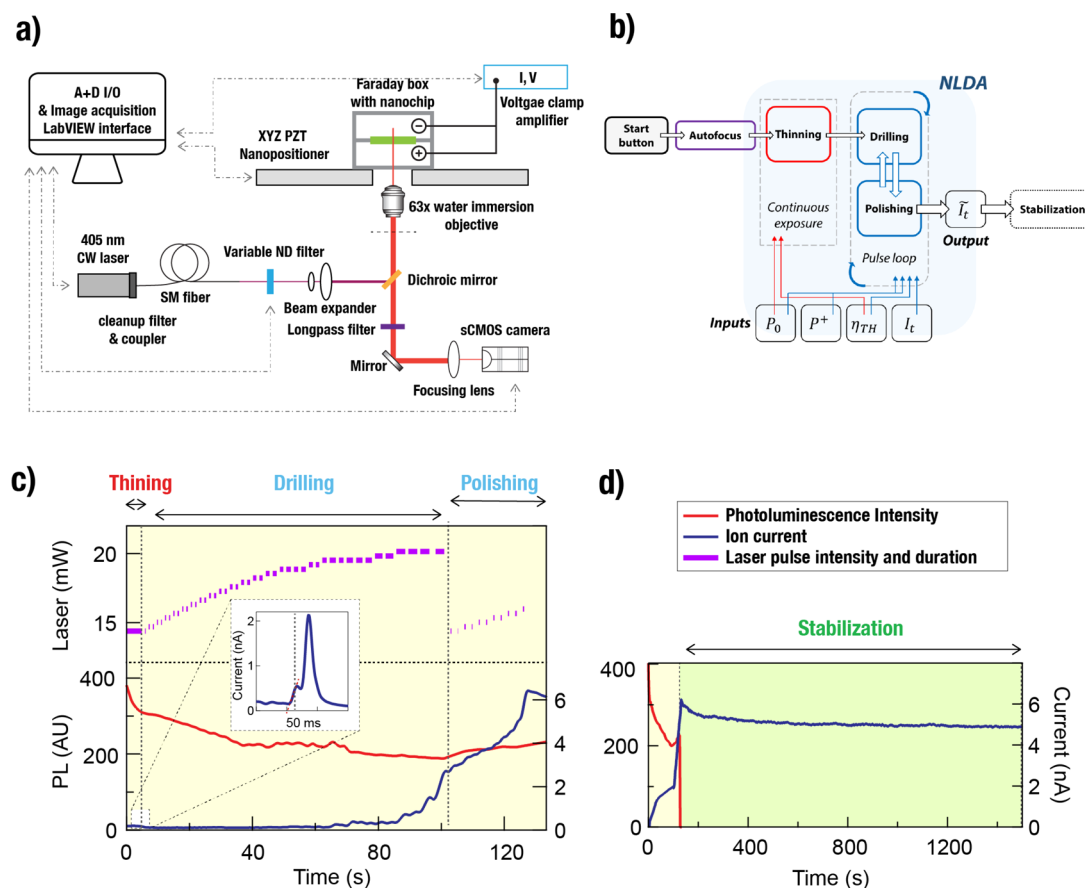


**Figure 2.** System design and laser drilling time traces. (a) Optical setup overview. The 405 nm continuous-wave laser is transmitted into the objective and focused on the membrane, where the reflected light is long-pass-filtered to measure photoluminescence (PL) by the sCMOS camera. The applied voltage, laser power, ND filters, and piezo stage are fully controlled by custom LabVIEW software (gray dashed arrows). The laser power is measured before the objective lens (black dashed line). (b) Schematic of the software designed to run the nanopore laser drilling algorithm (NLDA). The user sets the chip above the objective, positions the laser, and presses the start button. Then, the autofocus is activated, followed by the NLDA. The inputs (described in [Methods](#) section) are used to ensure convergence to the set nanopore value. (c) NLDA three main steps: thinning, drilling, and polishing. For display purposes only, the photoluminescence (PL, red) and current (blue) traces are smoothed and interpolated, thereby allowing a clear representation during the process (see [SI Figure 3](#) for the raw data). During the experiment, the PL decreases, indicating local thinning, while the current rises to the target open-pore current level. The pulse intensities and durations are represented by the violet trace. During the thinning step, the laser exposure is continuous. Starting from the drilling step, the laser is set to pulse mode, so the intensity trace is fragmented with increasing intensity and duration. In the polishing phase, the pulses are set to be short and weak since the current is susceptible to rapid increases. (d) Pore stabilization, demonstrating how the open-pore current is maintained over 20 min. The NLDA parameters used in this example, inputs:  $P_0 = 14.4$  mW,  $P^+ = 1\%$ ,  $\eta_{TH} = 4 \frac{nA}{s}$ ,  $I_t = 6$  nA; parameters:  $t_0 = 100$  ms,  $d = 1$  s,  $t_{IPD}^1 = 2$  s,  $t_{IPD}^2 = 1$  s,  $\gamma = 1.2$ ,  $\varphi_{TH} = 1$  nA,  $\rho_{TH} = 0.8$ ,  $\psi_{TH} = 1$  nA,  $R = 2$ .

shift in the  $z$  of even less than 100 nm may inhibit the LD process. To that end, we implemented a simple “search and find” focusing algorithm which converges within typically 10–15 s to the exact focus. [SI Figure 1](#) shows the main aspects of the autofocus process. First, the PL PSF is imaged and fitted by a Gaussian function to extract its amplitude and width. Then, the software moves the stage along the  $z$ -axis in a stepwise manner converging to the optimal focus (within 50 nm resolution) by maximizing the intensity. We define a minimization parameter,  $\delta$ , which corresponds to the normalized distance from the focus point, where the highest PL value is measured along the  $z$ -axis. Minimizing  $\delta$  equalizes the initial conditions for the subsequent drilling process, thus keeping the process robust and effective.

[Figure 2b](#) shows schematically the general flow of the LD process, which is controlled by the nanopore laser drilling algorithm (NLDA), integrated into our software (see [SI Figure 2](#) for the graphical user interface). The core algorithm was

designed to be a “one-button” program; i.e., the user loads the chip into its position, sets the laser in the desired  $X$ – $Y$  location, dials the desired nanopore size, and pushes a “GO” button. A pseudocode representation of the algorithm is provided in the [Supporting Information \(SI Algorithm 1\)](#) along with an explanation of the variables and parameters with their notations ([SI List 1](#)). The algorithm consists of several main blocks to handle the four steps of the LD process ([Figure 2b](#)): thinning, drilling, polishing, and stabilization. During the thinning phase, the membrane is continuously irradiated by the laser, resulting in a rapid local thinning which can be monitored by a corresponding decrease in PL intensity. This step is concluded when the software determines the formation of a pore based on monitoring the ion current time derivative,  $\delta I/\delta t$ . Pore drilling and polishing involve software modulated laser pulsing, which uses feedback Ohmic (DC) measurements of the pore conductance. Finally, pore stabilization occurs with the laser fully blocked. The rationale for this strategy is based

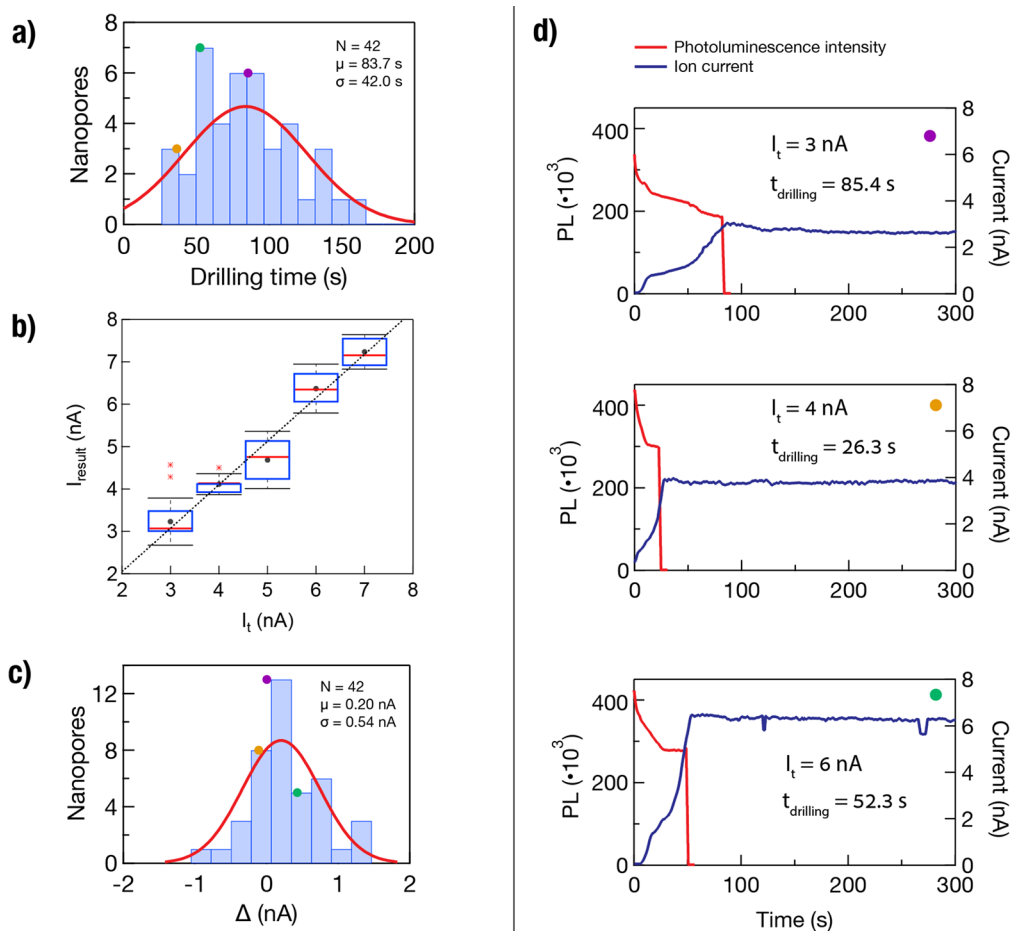


**Figure 3.** Samples of nanopore laser-drilling algorithm (NLDA) experiments. (a) Drilling time statistics. Histogram of the drilling time (not including stabilization) fitted using a Gaussian function. The mean and STD are indicated. (b) Final open-pore current  $I_{\text{result}}$  with respect to the set target size by the NLDA  $I_t$ . Whiskers show 1 STD, and outliers are marked with red asterisks. The gray line is linearly fitted to the group mean values (gray points) obtaining slope =  $1.026 \pm 0.062$ . (c) Histogram of the deviation of the final current from the target current  $\Delta = I_{\text{result}} - I_t$ . NLDA achieves an error of <5%. (d) Three representative NLDA examples taken from the population presented in panel c. Each one was set with a different  $I_t$  of 3 nA, 4 nA, and 6 nA, and obtained drilling times of 85.4 s, 26.3 s, and 52.3 s, respectively, from top to bottom. The stability of the nanopore open-pore current up to 5 min is presented for each trace.

on the observation that abrupt changes in the laser intensity (or large  $dP/dt$  values) induce  $\text{SiN}_x$  membrane charging or discharging, which in turn produces large jumps in the ion current followed by relaxation to a steady level. Therefore, to determine the unbiased Ohmic conductance, the software switches off the laser and waits for the current to stabilize.

In Figure 2c,d, we provide a typical account of the entire ssNP drilling process, which commences after the autofocus step is done. Figure 2c shows time traces of the laser intensity (violet), PL intensity (red), and the nanopore ion current (blue) during the first three steps of the process: membrane thinning, nanopore drilling, and nanopore polishing. Gaps in the laser intensity plot represent the time intervals in which the software turns off the laser. In this example, the user sets the target open-pore current ( $I_t$ ) to 6 nA (conductance of 20 nS). Once the NLDA determines that the set value has been reached, the system blocks the laser and begins the stabilization step, which typically lasts a few minutes. Typically, 2–3 min is sufficient for the stabilization, but in Figure 2d we show a continuous current measurement of 20 min to illustrate its long-term stability.

The main complication in LD in comparison to classical control systems is that at present it is only possible to expand

nanopores and not to controllably contract them. Therefore, the NLDA must converge to its target current on its first trial (“overshoots” are not allowed). Importantly, *maximum sensitivity* in the measurement, required in the thinning step, is achieved by continuously calculating the ion current *gradient* ( $\delta I/\delta t$ ) of a smoothed version of the current trace. The thinning step is terminated when the software detects the condition  $\delta I/\delta t \geq \eta_{\text{TH}}$  where  $\eta_{\text{TH}}$  is a predetermined threshold (e.g.,  $4 \frac{\text{nA}}{\text{s}}$ ) common to all chips in a given batch ( $\sim 200$  units).

This threshold, indicated in the inset of Figure 2c by a red line, signals the initial formation of the nanopore and the first penetration of electrolytes through the membrane. We observe an abrupt positive change in  $\delta I/\delta t$  values, used to trigger laser shutoff and the end of the thinning step. During the drilling and polishing steps, maximum accuracy is achieved by relying on DC Ohmic measurements of the pore conductance when the laser is off. Here, we apply laser pulses of about 100 ms, which are modulated by three parameters: (i) the pulse duration  $t_{\text{pulse}}$ , (ii) the pulse power  $P$ , and (iii) the interpulse delay time  $t_{\text{IPD}}$ . These parameters are tuned in real-time based on the ion-current measurements during the previous

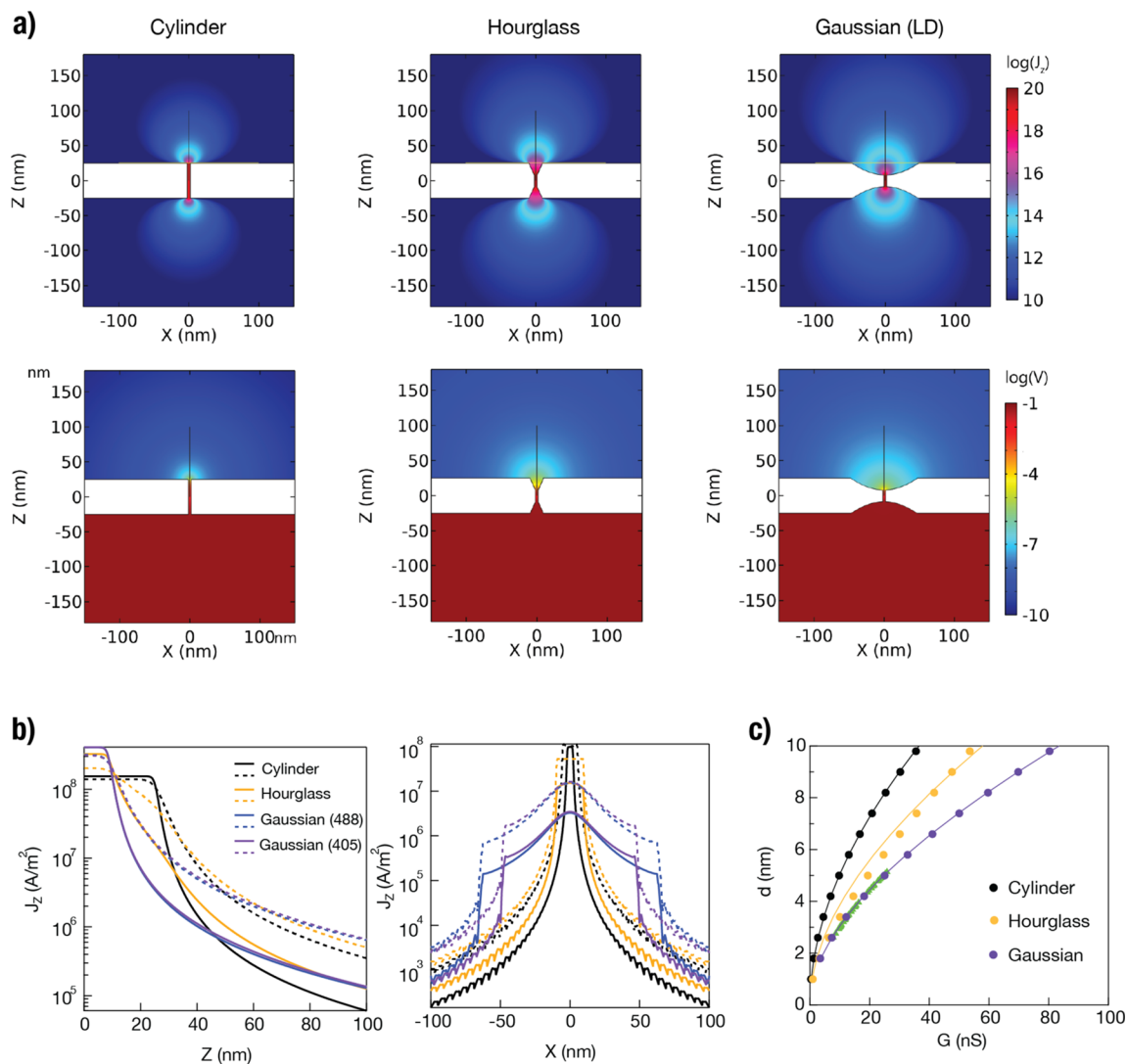


**Figure 4.** Numerical simulations of the spatial distributions of the electrical potential and current density in the vicinity of ssNPs having either a perfect cylinder, hourglass, or Gaussian form factors. (a) Simulated spatial distributions of the current density  $z$ -component ( $J_z$ , top row) and the electric potential (bottom row) distributions using the three form factors, as indicated ( $d = 4.2$  nm). The Gaussian form factor's thickness profile assumed a  $\lambda = 405$  nm Gaussian laser's beam. The  $X$  axis is obtained by cylindrical reconstruction. (b) Left and right panels show  $Z$  and  $X$  cross sections of the  $J_z$  calculated along the yellow and black lines in panel a, respectively. Solid and dashed lines correspond to 4.2- and 10.6-nm-diameter pores, respectively. (c) Numerical evaluation of the nanopore conductance  $G$  at different diameters  $d$  from the simulations. Data was globally fitted using eq 1 (solid lines) as described in the text. Green symbols represent the nanopore diameters obtained in the experiments from Figure 3 that were computed according to the measured conductance.

interpulse delays. The Methods section provides additional information regarding the laser pulsing control.

**Deterministic and Rapid Nanopore LD.** Using the fabrication method implemented by the NLDA, we could efficiently and deterministically drill stable ssNPs with an average size of 4 nm, as estimated by our model (see below) and validated by translocation experiments. Once the NLDA was fully optimized, the mean drilling time was just a few minutes, equivalent to or shorter than previous reports of laser-based ssNP drilling<sup>30,31,34</sup> and substantially shorter than other ssNP drilling methods when considering the deterministic size control feature. In Figure 3, we present a summary of 42 NLDA experiments, each resulting in a drilled ssNP. The overall drilling time (including thinning, drilling, and polishing) is shown in Figure 3a. We did not include the stabilization time, as this is an optional step that is often used with all other nanopore drilling strategies. The histogram is fitted using a

normal distribution, with a mean value of 84 s and a STD of 42 s. The large STD of the drilling time can be attributed to the fact that each of the chips was manually assembled in the holder, and in addition, each chip was selected from a different area in the wafer where slight variances in membrane thickness and Si/N composition exist, both of which impact the drilling time of the NLDA.

The boxplot in Figure 3b displays the NLDA performance for different set target values  $I_t$ . Each of the boxes represents a different target for a group of experiments with respect to the actual final open-pore current obtained,  $I_{\text{result}}$ . Each box is statistically separated from its neighbors, where overlapping is found only outside of the majorities. In addition, it demonstrates the process uniformity, where the behavior is similar, regardless of the fabricated nanopore size. The gray line is a linear fit between the  $I_{\text{result}}$  and  $I_t$  having a slope =  $1.026 \pm 0.062$ . Figure 3c displays the overall performances (as

in Figure 3a), showing the deviation of  $I_{\text{result}}$  from  $I_t$ . As can be seen, based on the statistics of 42 nanopores drilled using a range of  $I_t$  from 2 nA to 8 nA, a mean error of 0.2 nA (equivalent to  $\sim 0.67$  nS) between the set value and the stabilized open-pore current is obtained. This corresponds to a less than 5% mean error in achieving the set point current or a roughly 2.5% error in the corresponding calculated ssNP diameter. Three typical ssNP LD traces are shown in Figure 3d having an  $I_t$  of 3 nA, 4 nA, and 6 nA from top to bottom, respectively (all measured with  $V = 300$  mV). Notably, NLDA achieved the desired levels within 26 to 86 s, before the pores were left for a few minutes of stabilization.

### Investigating the NLDA-Fabricated ssNP 3D Shape.

After developing the NLDA for rapid and deterministic ssNP fabrication, we asked whether the special pore form-factor produced by the Gaussian laser beam has an impact on the nanopore's performance. Nanopore conductance is generally affected by both the in-pore resistance and the access resistance, modeled according to

$$G = \frac{I}{V} = \left( \frac{4h_{\text{eff}}}{\pi d^2} + \frac{1}{d} \right)^{-1} \sigma \quad (1)$$

where  $h_{\text{eff}}$  is the membrane effective thickness,  $d$  is the nanopore diameter, and  $\sigma$  is the solution specific conductivity. Equation 1 represents a simplified approximation of the physical ssNP shape as a perfect cylinder and ignores additional effects such as surface roughness and surface charge. Nevertheless, it is practically useful in providing an idea of the ssNP dimensions based on the measured conductance and has often been used to approximate the ssNP diameter. Importantly, however, not only the Ohmic characteristics of the nanopore determine its ability to efficiently sense biomolecules. In addition to the pore conductance, the electrical field distribution outside the pore  $\vec{E}(z, r)$  affects the rate at which charged biomolecules are transported to the nanopore prior to their entry, hence playing an important role in the functionality of the device.<sup>7</sup> Therefore, when determining the ssNP performance, it is essential to consider not only its diameter and the membrane thickness, but also its physical shape beyond the narrowest constriction.

Previous investigations of TEM-drilled nanopores suggested an approximately hourglass form factor with a cone angle of roughly  $30^\circ$  and an effective thickness of roughly  $1/3$  of the membrane nominal thickness.<sup>35</sup> For LD ssNPs, TEM-based thickness profiling of the membrane demonstrated that the membrane thinning follows a Gaussian profile having the dimensions of the tightly focused laser beam.<sup>30</sup> As photo-induced etching may occur symmetrically on both sides of the membrane, it is likely that the actual nanowell shape formed by the laser includes two back-to-back Gaussian "bowls" connected by the nanopore. This structure resembles to some extent the "hourglass" shape of nanopores created by the TEM drilling, except with a much wider opening.

To gain deeper insight into the LD ssNP properties, we performed numerical simulations using COMSOL Multiphysics (COMSOL, Inc.) of the electrical potential  $V(z, r)$  and electrical field via the ion current density vector  $\vec{J}(z, r) = \sigma \vec{E}(z, r)$ , as shown in Figure 4a and in SI Figure 4. To provide context to our simulations, we compared it with a naive (perfect cylinder) and hourglass nanopore of similar dimensions, as indicated. Line profiles of the  $z$ -components of  $\vec{J}(z, r)$  suggest that the LD ssNP electrical field decays away

from the ssNP ( $z$  axis and  $r = 0$ ) in a similar fashion as the TEM drilled ssNP (hourglass), as shown on the leftmost panel on Figure 4b. However, in the pore vicinity the electrical field  $z$ -component extends to a much broader range as compared with the other form factors, as shown in the Figure 4b right panel, suggesting potentially better biomolecule focusing and capture. We note, however, that an experimental confirmation of this observation would require extensive investigation of the precise nanopore form factors using TEM tomography or alternative approaches that are beyond the scope of this study.

The numerical simulations of the ion current density may be used to evaluate the accuracy of the simplified theoretical description presented in eq 1, for each of the nanopore form factors (cylinder, hourglass, and Gaussian). To that end, we used the numerical simulations to calculate the open-pore current (see Supporting Information section IV) and divided by the full potential drop to obtain the conductance  $G(d)$  as a function of the pore diameter. Our results are presented in Figure 4c with the axes inverted to show  $d(G)$ , as the nanopore conductance is readily measured in experiments, whereas its diameter is not as easily determined. Using eq 1, we globally fit the three data sets, fixing  $h_{\text{eff}}$  of the naive (a perfect cylinder) pore to the membrane nominal thickness (50 nm) and forcing a single value for the specific solution conductance. From the fits, we obtained  $\sigma = 26.86 \pm 0.54$  ( $\Omega \text{ nm}$ )<sup>-1</sup>;  $h_{\text{eff}}(\text{HG}) = 28.6 \pm 0.8$  nm;  $h_{\text{eff}}(\text{LD}) = 17.5 \pm 0.5$  nm. Returning to Figure 3, we added on top of the numerically simulated LD pore the 42 experimentally measured NLDA nanopores. This allowed us to estimate the pore diameter from the measured conductance subject to the assumptions made in the numerical simulation. As shown in the Figure 4c, the nanopore sizes were between 2.5 and 5 nm, within the expected range based on the protein translocation results.

**Translocation Analysis of SDS-Denatured Carbonic Anhydrase Proteins.** To validate the ability of the NLDA to fabricate functional ssNPs, we measured SDS-denatured Carbonic Anhydrase II (CA2) translocations right after LD. CA2 is a 260-amino-acid-long protein (pI 6.87), which is negatively charged in the alkaline LD buffer. The protein was added to the *cis* chamber of the setup with a final concentration of 10 nM. Importantly, to maintain the proteins' denatured state, translocations were performed in the presence of SDS (see Methods section for more details). Figure 5a displays a characteristic NLDA trace achieving a stable 13 nS ssNP (about 4 nA at 300 mV), in less than 30 s. According to the LD conductance simulations (Figure 4c) this corresponds to a  $\sim 3.5$  nm ssNP diameter. After  $\sim 11$  s of membrane thinning, the program started the pore polishing, terminating the process after 7 laser "pulses" when achieving the target open-pore current ( $I_t = 4$  nA). Inset displays bright light images showing the PL spot before pore formation (left) and the same area after pore formation (right, laser off). The nanopore measured  $I-V$  curve is shown in SI Figure 5. As in the NLDA process, the next steps take place under voltage of  $V = 300$  mV as well. Right after the ssNP stabilized, we added the protein and SDS sample to the *cis* chamber and recorded translocation events for about 20 min. We noted that upon analyte addition the open-pore current ( $I_0$ ) slightly increased to about 4.6 nA and remained stable throughout the experiment with  $I_0 = 4.65 \pm 0.05$  nA (mean  $\pm$  STD). Figure 5b top panel displays  $I_0$  measured in between the events. The bottom panel in Figure 5b displays an event diagram (the fractional current  $I_B$  versus event dwell time  $t_D$  shown in

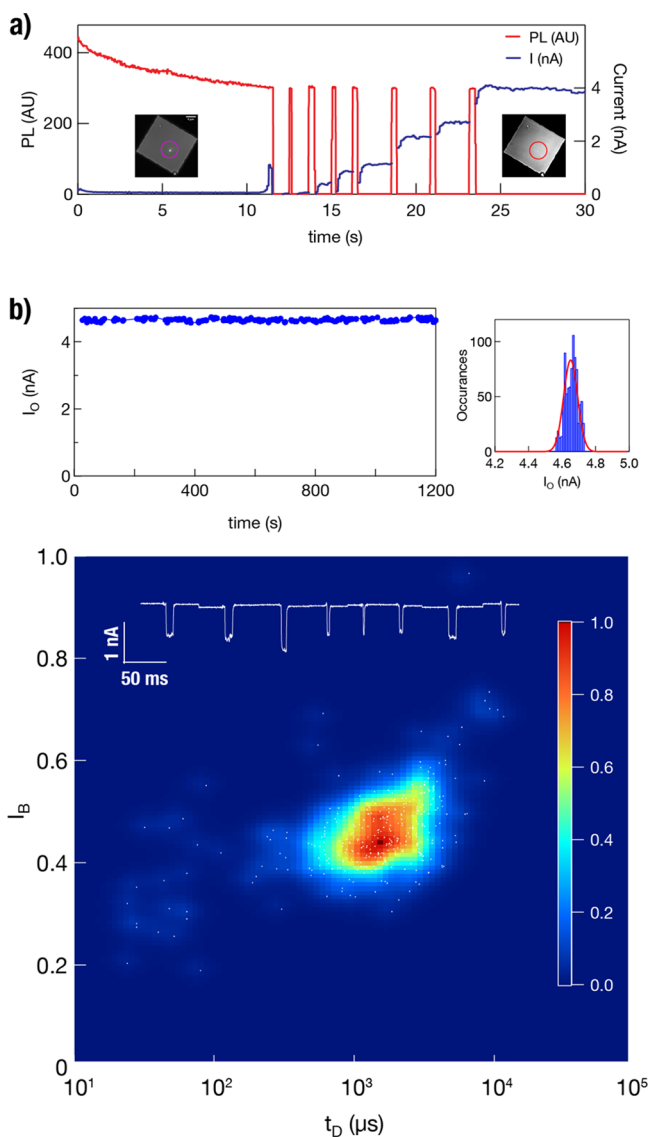


**Figure 5.** SDS-denatured carbonic anhydrase II protein (CA2) translocations using a laser-drilled nanopore. (a) NLDA process, showing the PL and ion current traces during thinning and drilling. The processes lasted 30 s, where the target open-pore current was  $I_t = 4$  nA. Inset shows bright light before pore formation (PL spot visible, violet circle) and thinned area after drilling (laser off, red circle). (b) Nanopore stability during translocations of SDS-denatured CA2. Top: After addition of the CA2 analytes and SDS molecules, the open-pore current ( $I_0$ ) increased to 4.65 nA and remained stable during at least 20 min of recording the CA2 translocations. Right panel shows  $I_0$  values in-between the events and its histogram fitted to a Gaussian function  $4.65 \pm 0.05$  nA (mean  $\pm$  STD). Bottom: a scatter plot of the fractional blocked current and dwell time  $t_D$  for the 437 translocation events collected in about 20 min. The scatter plot is superimposed on a heat map representing the 2D histogram density. Inset shows typical translocation events.

logarithmic scale) consisting of 358 translocation events plotted on top of a heat map representing the 2D histogram density. As can be seen, we obtained relatively deep and long translocation dwell times, suggesting that the nanopore is only slightly larger than the SDS denatured polypeptide chain. Histograms of the fractional current blockage and dwell time yield mean values of  $0.43 \pm 0.04$  and  $900 \pm 95$   $\mu$ s, respectively

(SI Figure 6). These values qualitatively agree with a nominal thickness of the SDS denatured polypeptide chain of about 2 nm. Notably, since the CA2 pI is  $\sim 6.87$ , when using our pH 10 buffer we expected to obtain a beneficial negative charge that can assist with drawing the proteins from the *cis* reservoir to the *trans* one, according to the applied electric field. The relatively long measured dwell time of the proteins may suggest a relatively small charge/mass ratio and/or preferable interactions with the ssNP wall, presumably mediated by the SDS molecules.

**Photochemical Etching Mechanism.** The ability to consistently fabricate large numbers of ssNPs in an unattended manner facilitates further investigation into the photochemical laser etching process. Our previous studies indicated that low-intensity/time-efficient LD requires Si-rich  $\text{SiN}_x$  membranes and alkaline conditions (i.e., pH 10).<sup>31</sup> When the laser energy is greater than the material bandgap energy, the laser irradiation generates electron–hole pairs within the  $\text{SiN}_x$  surface and charge transfer at the liquid–solid interface. This surface charging catalyzes a rapid photochemical etching of the membrane at the beam center. The etching progresses into the membrane resulting in a shape that roughly replicates the Gaussian beam profile. Importantly, however, as the thinning process progresses, the interfacial charges from the two sides of the membrane may gradually repel each other, creating a charge depletion zone. The localized charge depletion zone slows down the etching kinetics, prior to the eventual formation of the nanopore, as schematically depicted in Figure 6a.

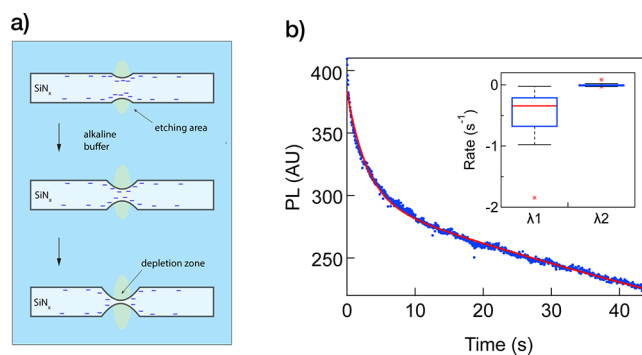


**Figure 6.** (a) Schematic (not to scale) model for the photochemical  $\text{SiN}_x$  membrane thinning leading to pore formation. A charge depletion zone is generated by the thinning process. (b) Characteristic photoluminescence (PL) intensity trace during membrane thinning showing a fast decay followed by a slow decay. The processes are approximated by a sum of two decaying exponentials with rate constants  $\lambda_1$  and  $\lambda_2$ . Analysis of 15 membrane thinning traces consistently yield two decaying rates differing by 2 orders of magnitude (inset, boxplot is defined as in Figure 3).

To check this hypothesis, we analyzed the photoluminescence time traces during the membrane thinning stage of 15 LD trials, as defined by the NLDA. We observed a characteristic rapid reduction in PL intensity, followed by a slower decay over longer times (Figure 6b). We empirically fitted the processes by a sum of two decaying exponential functions, which yielded two clearly distinct rate constants ( $\lambda_1 = 0.343 \pm 0.008$   $\text{s}^{-1}$  and  $\lambda_2 = (60.0 \pm 0.7) \times 10^{-4}$   $\text{s}^{-1}$  differing by more than 2 orders of magnitude (additional examples for such traces are found in SI Figure 7). Upon the creation of a

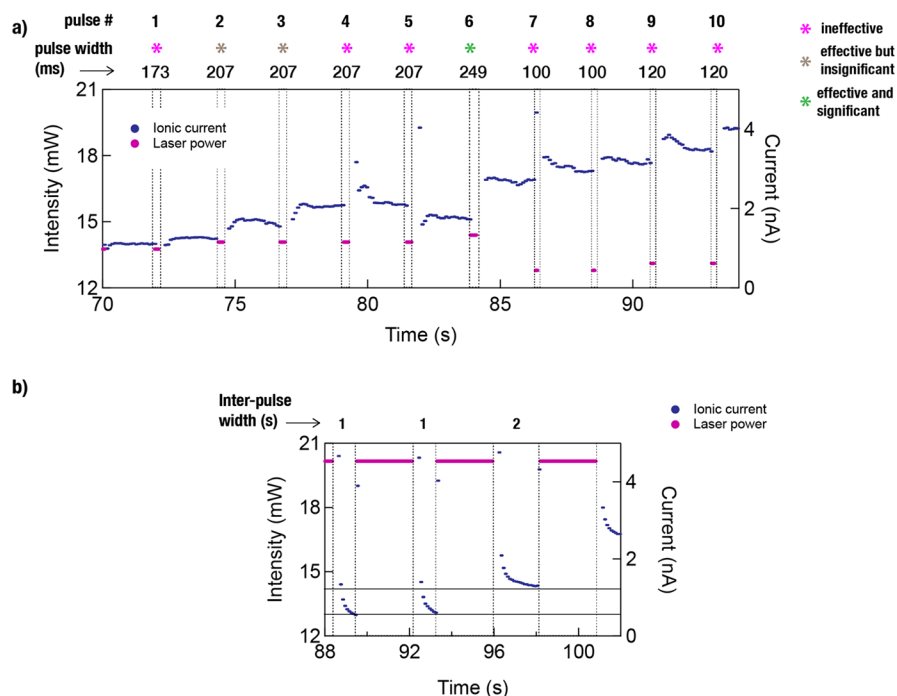


**Figure 7.** NLDA pulse control scenarios. (a) Example for pulse intensity ( $P$ ) and duration ( $t_{\text{pulse}}$ ) modulation. The 10 pulses demonstrate the differences between “effective and significant” (green asterisks), “effective but insignificant” (gold), or “ineffective” (pink). After each two consecutive ineffective pulses ( $R = 2$ ), the intensity and the pulse duration grow by  $P'$  and  $\gamma$ , respectively. After each effective and significant pulse, the power and duration are reduced to  $P_0 = 12.8$  mW and  $t_0 = 100$  ms, respectively. (b) Interpulse delay duration switching example. The periods between pulses are modified by the  $\varphi_{\text{TH}} = 1$  nA threshold. The first and second interpulse duration last for  $\tau_{\text{IPD}} = 1$  s, allowing relatively fast drilling, whereas the third, which is above  $\varphi_{\text{TH}}$ , lasts for  $\tau_{\text{IPD}} = 2$  s, enabling measurement of the current in a precise, fine-tuning polishing mode.

nanopore (signaled by the ion current jump), the membrane thinning step is terminated and the nanopore expansion/polishing starts. We checked if nanopore expansion proceeds without the laser by keeping the laser off while monitoring the ion current flow under a constant applied voltage (300 mV) typically used in translocation measurements. Over the course of  $>10$  min, we did not observe any change in the ion current ( $n = 3$ ), hence ruling out the possibility of purely electrically driven pore expansion. In contrast, when short laser pulses are applied, we observe larger spikes in the measured ion current. Presumably, the localized laser induces the creation of electron–hole pairs, but the different mobilities of two carriers generate a local electromotive force (EMF) in the radial direction (Dember effect) that acts as a battery leading to the observed current spikes.<sup>36</sup> Moreover, the local and transient charging of the nanopore interfaces facilitates the process of photochemical etching of the  $\text{SiN}_x$  and the controlled enlargement of the nanopore, which would be otherwise too abrupt to finely control.

## CONCLUSIONS

With the rapid growth of nanopore sensing in basic life sciences and in clinical diagnostics applications, there is an unmet need for a fast, highly deterministic, and broadly accessible nanopore fabrication method. Laser-based nanopore drilling is a promising technique for fast *in situ* nanoscale material etching in buffered aqueous solutions. Sophisticated devices for biomolecule sensing applications may involve the integration of the nanopore sensor in fluidic chambers used for sample preparation and delivery. Hence, the flexibility of forming the pore at the desired destination location using a

focused laser beam is of high practical value.<sup>37</sup> A general outstanding issue of many of the nanopore drilling methods has been the method’s ability to rapidly and reproducibly deliver the desired pore size without user intervention. To accomplish this goal, effective and real-time feedback indicators such as the nanopore ion current and PL intensity can be implemented to ensure a high probability convergence of the process to the set values. To that end, the LD process offers sufficient versatility as the photon energy, pulse duration, and environmental conditions such as the buffer pH can be employed as a wide bandwidth of control values.

Here, we have demonstrated that a multistep control algorithm (called NLDA), coupled to an electromechanical system, can be realized to achieve fast and deterministic nanopore fabrication with sizes in the range of 2.5 to 5 nm, which are useful for sensing DNA and protein molecules. Notably, our system is not limited to this size range, and we anticipate that both smaller and larger pores can be created with minor adjustment to NLDA. Our method has been tested using a number of different  $\text{SiN}_x$  deposition batches and performed well even when the exact initial membrane thickness varied significantly. We noticed, however, that exact z-focusing of the beam and mechanical stability of the stage during the drilling are critical factors that must be preserved to ensure a high success rate. Despite variability in the overall drilling time of NLDA (attributed primarily to variable initial physical properties of the fabricated solid-state free-standing membranes), we noted that the typical drilling time remained well below 2 min, roughly an order of magnitude faster than TEM- or CDB-based drilling. Moreover, the flexibility of forming the nanopore at any specific location

along the membrane *in situ* presents an additional value to the method. Future improvements of the LD method may include a compact apparatus and higher drilling throughput, further paving the way toward a broad adoption of sSNPs in basic research and industry.

## METHODS

**NLDA Pulse Control.** Figure 7a shows a set of 10 laser pulses during the nanopore drilling step, and the resulting nanopore current. The laser pulse widths are indicated at the top. After each pulse, the laser is blocked for time  $t_{\text{IPD}}$ , and the system's open-pore current is stabilized and measured. With each successive pulse, the current is either increased or remains roughly at the same level. See Table 1 and SI List 1 for the NLDA variable description.

**Table 1. NLDA Inputs and Parameters**

input/parameter	notation	description
NLDA inputs (Set by the user)	$P_0$	Initial laser power
	$P^+$	Laser power increment factor
	$\eta_{\text{TH}}$	Current gradient threshold
Optimized parameters (Should not be changed between batches)	$I_t$	Target open-pore current
	$t_0$	Initial pulse duration
	$d$	Delay before applying the $\eta$ condition during the pulse operation
	$t_{\text{IPD}}^l$	Long interpulse delay
	$t_{\text{IPD}}^s$	Short interpulse delay
	$\gamma$	Pulse time geometrical increment factor
	$\varphi_{\text{TH}}$	Polishing threshold
	$\rho_{\text{TH}}$	Effectiveness threshold
	$\psi_{\text{TH}}$	Significance threshold
	$R$	Consecutive ineffective pulses limit

The main control principle implemented in the NLDA involves decision making based on analysis of the drilling past trajectory (as opposed to a single data point), performed in real-time by the setPulseParameters (sPP) function (Supporting Information – SI Algorithm 1). Two parameters control the next pulse characteristics: the effectiveness and significance of the previous pulse, denoted  $\rho$  and  $\psi$ , respectively. These parameters are used to classify the pulse into one of three categories: “effective and significant”, “effective but insignificant”, or “ineffective”. Examples of this classification are shown in Figure 6a by asterisks (green, gold, and pink, respectively).

The effectiveness parameter, defined as  $\rho \equiv \frac{\mu^{N-1}}{I_N}$ , where  $\mu^{N-1} \equiv \frac{1}{N-1} \sum_{n=1}^{N-1} I_n$  and  $N$  is the last pulse, quantifies the change in the current after the last pulse in comparison to several previous pulses. The  $R$  parameter (e.g.,  $R = 2$ ) determines the number of previous pulses to be considered and serves as a limit for consecutive ineffective pulses. The algorithm keeps in memory the currents of the consecutive ineffective pulses, as  $\mu^{N-1}$  suggests, and when this number is crossed, i.e.,  $N > R$ , the sPP function alters  $t_{\text{pulse}}$  and  $P$  to be used in the next pulse. A pulse is assumed to be effective when the effectiveness parameter meets the threshold condition  $\rho \leq \rho_{\text{TH}}$  (e.g.,  $\rho_{\text{TH}} = 0.8$ ). The significant parameter is defined as  $\psi \equiv I_N - \mu^{N-1}$ , and similarly, a pulse is considered significant when  $\psi > \psi_{\text{TH}}$  (e.g.,  $\psi_{\text{TH}} = 1$  nA). If a pulse is found to be effective but insignificant, sPP will keep the same laser intensity and duration for the next pulse. This occurred after the second pulse in Figure 3b, where 207 ms duration was applied in the third pulse as well (note the mild current level rise between these pulses). On the contrary, consecutive ineffective pulses will result in increments of these properties, as in the shift between the fourth and fifth pulses toward the sixth one, where the duration grows to 249 ms (in this case  $R = 2$ ). The increment is set by a factor

$\gamma$  (e.g.,  $\gamma = 1.2$ ) that alters the duration in geometrical growth (i.e.,  $t_{\text{pulse}} \leftarrow \gamma t_{\text{pulse}}$ ), which can result in a steep pulse-duration increment in cases of long ineffective pulse series. On the other hand, the intensity grows in a linear manner (i.e.,  $P \leftarrow P + P^+$ , where  $P^+$  is the power increment factor with units of % measured from the maximum laser power, e.g.,  $P^+ = 1\%$ ), to keep mild steps of power over the duration geometrical growth. Notice that the seventh and tenth pulses are considered ineffective despite the observable growth in the current level, which is a result of the ratio definition of  $\rho$ . Accordingly, at higher current levels the threshold becomes much less permissive. This causes a linear increase in the intensity when the pore is already open yet has not reached its final targeted size. Thus, it usually happens at the beginning of an ineffective series when the duration geometrical increment is still at its short negligible period (mild increments). Such behavior is found to be beneficial to the polishing stage. This incremental behavior ceases when a significant pulse appears. Then, the significance parameter  $\psi$  crosses a threshold value ( $\psi > \psi_{\text{TH}}$ ), which causes the duration and intensity to be restored back to their initial low values (e.g.,  $P_0 = 14.4$  mW and  $t_0 = 100$  ms) and ensure pulsing in a fine-tuning mode. This is demonstrated in Figure 6a, where a significant current rise following the sixth pulse is considered, resulting in the shortening of the seventh pulse back to 100 ms. This behavior of substantial pore expansion is often visible in the transition between the *drilling* and *polishing* stages, as demonstrated in Figure 2c, where the pulses are becoming weaker and shorter. Note that Figure 6a represents only an example taken from a specific experiment, where in fact each of the experiments results in a different trajectory of pulses with diversity of durations and intensities, according to the initial conditions.

Another performance that the NLDA alters is the duration of  $t_{\text{IPD}}$ , i.e., how much time the algorithm waits before sampling  $I_N$ . This simple yet important distinction sets the threshold between the *drilling* and *polishing* modes. By passing the “polishing threshold”  $\varphi_{\text{TH}}$ , an optimized parameter defined with an absolute current level, the NLDA switches between two  $t_{\text{IPD}}$  values: short  $t_{\text{IPD}}^s$  and long  $t_{\text{IPD}}^l$  for *drilling* and *polishing*, respectively. In this way, the NLDA alternates between two types of behaviors: the short interpulse delay allows the overall process to run faster, whereas the long interpulse delay permits a more precise measurement of the ion current  $I$ , after waiting the extended time. This might alternate several times in different manners during each specific pulse trajectory, but it usually will end with a series of consecutive polishing pulsing, as Figure 2c suggests. Figure 6b displays the transition section between *drilling* and *polishing* triggered by crossing the threshold  $\varphi_{\text{TH}} = 1$  nA and the resulting doubling of  $t_{\text{IPD}}$  from 1 to 2 s between the second and third pulses.

**Membrane Fabrication and Device Assembly.** Four-inch  $\sim 350$ - $\mu\text{m}$ -thick silicon wafers were coated by LPCVD with layers of  $\sim 500$  nm silicon dioxide ( $\text{SiO}_2$ ) and  $\sim 50$  nm  $\text{SiN}_x$  from both sides. The  $\text{SiN}_x$  refractive index was measured by ellipsometry (FS-1, Film sense) and confirmed to be  $n = 2.29 \pm 0.01$ . Each wafer was spin-coated with a photoresist (AZ1518, Micro chemicals) applied by direct photolithography with a custom window-pattern mask (written with Microwriter ML3, Durham Magneto Optics Ltd.), and finally developed (S035S, Novo). Then, the first  $\text{SiN}_x$  layer was etched and removed by reactive ion etching (RIE, diener electronic PCCE machine). The exposed  $\text{SiO}_2$  was dissolved with buffered oxide etch (BOE) to complete the hard mask. Then, KOH was used to etch the Si layer all the way through for 19 h @ 57 °C in a custom-built bath for maintaining the temperature and flow in the solution. Another BOE etching was applied to remove the second  $\text{SiO}_2$  layer, resulting in a  $\sim 50$  nm  $\text{SiN}_x$  free-standing membrane. For the  $\text{TiO}_2$  samples, the membrane was coated using atomic layer deposition (ALD) according to the manufacturer's recipe (GEMStar XT) to obtain a 10 nm layer (applied before the KOH step).

Each chip is mounted onto a Teflon holder by PDMS, which is used to isolate the two chip sides. The holder is placed in a Teflon cell to form two chambers of separated aqueous solution. A custom seating is installed above the objective to hold the Teflon cell, where its bottom side is glued to a thin glass cover slide that allows the laser to be focused on the chip through the aqueous solution.

**Optical Setup.** A custom-made confocal setup was used for the NLDA as described in Figure 2a. The excitation path includes the Toptica iBeam smart lasers (488 or 405 nm, including cleanup filters) and Thorlabs neutral density filters and mirrors. All are directed through a Zeiss Axiovert 200M microscope frame into a Zeiss Apochromat water objective (NA = 1.15, 63 $\times$ ) which focuses the laser into a diffraction-limited spot. In the emission path, the fluorescence and reflected laser from the sample are collected by the same objective, where a Semrock dichroic mirror of 405 nm (Di01-R405/488/532/635–25 $\times$ 36), and 430 or 488 nm (laser dependent) long-pass filter (FF01-430 or -496/LP-25) are used to selectively capture the PL and measure it by an Andor Zyla 4.2 sCOMS camera (PL images are sampled at 33.33 Hz). The laser intensity was measured by a Thorlabs power meter before the objective lens. A PI P-561 piezo stage controlled by an E-710 controller is installed above the objective and is used to move the nanopore device in submicrometer steps laterally and axially. An Axon Axopatch 200B amplifier is used to measure the electrical current (sampled at 125 kHz) and apply voltage across the membrane. All the instruments and devices are controlled by a custom LabVIEW software, connected through serial connections and/or digital/analog input and outputs of NI PCI-6602 and NI PCI-6154.

**Aqueous Solution Preparation.** Drilling-only experiments were performed in a salt solution containing 1 M KCl and 0.02 M sodium bicarbonate-based buffer (18:22 ratio of sodium bicarbonate and sodium carbonate) titrated to pH 10. For *in situ* translocation experiments, 173  $\mu$ M sodium-dodecyl sulfate (SDS) was added to the buffer.

**TEM Imaging and EDS Analysis.** *EM Imaging:* High-resolution images were acquired with an FEI Titan Themis Cs-Correct HR-S/TEM. The low loss energy spectrum was measured in scanning transmission electron microscopy (STEM) in increments of 20 nm and was used to automatically generate relative thickness maps using Digital Micrograph software (Gatan). *Composition Analysis:* Chemical mapping of the SiNx membranes was performed using EDS (Dual Bruker XFlash6) and STEM based on core-loss EELS. The EDS quantification was done using Velox (Thermo Fisher) and EELS quantification was done using the Digital Micrograph software (Gatan).

**Signal and Image Processing.** All post-processing of the LD experiments and image processing during laser focusing were computed with a custom Matlab (Mathworks) code, as described in the Supporting Information Section II. All graphs were plotted and fitted in IgorPro (Wavemetrics).

**Software Programming.** Control and automation software including the NLDA algorithm (SI Algorithm 1) was programmed in LabVIEW (National Instruments).

**Sample Preparation.** The protein sample was prepared at high concentration which was further diluted by 100-fold for the nanopore experiment. For preparing a denatured protein sample, a standard protocol was followed: 10  $\mu$ g/mL of the carbonic anhydrase protein was dissolved into 1 M PBS buffer. To disrupt the disulfide interaction of the cysteine residue, 5 mM of TCEP was added to the reaction mixture. 350  $\mu$ M of ionic surfactant SDS, which is used for protein denaturation in combination with heat, was also added to the reaction mixture. The reaction was allowed to shake for 30 min at 25  $^{\circ}$ C and 300 rpm. Furthermore, to denature the protein, the reaction mixture was heated at 90  $^{\circ}$ C for 5 min. The reaction was allowed to cool again to room temperature before it was added to the nanopore device *cis* chamber for the experiment.

**Numerical Simulations.** Numerical simulations were conducted *via* Comsol Multiphysics (Comsol Inc.) to solve the Nernst–Planck–Poisson equations in a finite element method. See the Supporting Information for comprehensive details.

## ASSOCIATED CONTENT

### Supporting Information

The Supporting Information is available free of charge at <https://pubs.acs.org/doi/10.1021/acsnano.1c03773>.

Supplementary figures, signal and image processing details, the NLDA pseudo code and notations table, numerical simulations implementation details, table summary of the laser drilling enhancements (PDF)

## AUTHOR INFORMATION

### Corresponding Author

Amit Meller – Department of Biomedical Engineering, Technion-IIT, Haifa 32000, Israel; [orcid.org/0000-0001-7082-0985](https://orcid.org/0000-0001-7082-0985); Email: [ameller@technion.ac.il](mailto:ameller@technion.ac.il)

### Authors

Eran Zvuloni – Department of Biomedical Engineering, Technion-IIT, Haifa 32000, Israel

Adam Zrehen – Department of Biomedical Engineering, Technion-IIT, Haifa 32000, Israel

Tal Gilboa – Department of Pathology, Brigham and Women's Hospital, Harvard Medical School, Boston, Massachusetts 02115, United States; Wyss Institute for Biologically Inspired Engineering, Harvard University, Boston, Massachusetts 02115, United States; [orcid.org/0000-0001-8172-7786](https://orcid.org/0000-0001-8172-7786)

Complete contact information is available at:

<https://pubs.acs.org/doi/10.1021/acsnano.1c03773>

### Author Contributions

The manuscript was written through contributions of all authors. All authors have given approval to the final version of the manuscript.

### Notes

The authors declare no competing financial interest.

## ACKNOWLEDGMENTS

We thank Y. Rozevsky, N. Freundlich, and N. Soni for assistance in sample preparation, and Y. Kaufman for support in the TEM analysis. This project has received funding from the European Research Council (ERC) No. 833399 (Nano-Prot-ID) and ERC-PoC No. 966824 (OptiPore) both under the European Union's Horizon 2020 research and innovation programme grant agreements.

## REFERENCES

- (1) Deamer, D.; Akesson, M.; Branton, D. Three Decades of Nanopore Sequencing. *Nat. Biotechnol.* **2016**, *34* (5), 518–524.
- (2) Dekker, C. Solid-State Nanopores. *Nat. Nanotechnol.* **2007**, *2* (4), 209–215.
- (3) Mathe, J.; Aksimentiev, A.; Nelson, D. R.; Schulten, K.; Meller, A. Orientation Discrimination of Single-Stranded DNA Inside the Alpha-Hemolysin Membrane Channel. *Proc. Natl. Acad. Sci. U. S. A.* **2005**, *102* (35), 12377–12382.
- (4) Hall, A. R.; Scott, A.; Rotem, D.; Mehta, K. K.; Bayley, H.; Dekker, C. Hybrid Pore Formation by Directed Insertion of  $\alpha$ -Haemolysin Into Solid-State Nanopores. *Nat. Nanotechnol.* **2010**, *5* (12), 874–877.
- (5) Li, W.; Bell, N. A. W.; Hernández-Ainsa, S.; Thacker, V. V.; Thackray, A. M.; Bujdoso, R.; Keyser, U. F. Single Protein Molecule Detection by Glass Nanopores. *ACS Nano* **2013**, *7* (5), 4129–4134.
- (6) Meller, A.; Nivon, L.; Branton, D. Voltage-Driven DNA Translocations Through a Nanopore. *Phys. Rev. Lett.* **2001**, *86* (15), 3435–3438.
- (7) Wanunu, M.; Morrison, W.; Rabin, Y.; Grosberg, A. Y.; Meller, A. Electrostatic Focusing of Unlabelled DNA Into Nanoscale Pores Using a Salt Gradient. *Nat. Nanotechnol.* **2010**, *5* (2), 160–165.

- (8) Squires, A.; Atas, E.; Meller, A. Nanopore Sensing of Individual Transcription Factors Bound to DNA. *Sci. Rep.* **2015**, *5*, 1–11.
- (9) Rozevsky, Y.; Gilboa, T.; van Kooten, X. F.; Kobelt, D.; Huttner, D.; Stein, U.; Meller, A. Quantification of mRNA Expression Using Single-Molecule Nanopore Sensing. *ACS Nano* **2020**, *14* (10), 13964–13974.
- (10) Rauf, S.; Zhang, L.; Ali, A.; Liu, Y.; Li, J. Label-Free Nanopore Biosensor for Rapid and Highly Sensitive Cocaine Detection in Complex Biological Fluids. *ACS Sensors* **2017**, *2* (2), 227–234.
- (11) Wang, Y.; Zheng, D.; Tan, Q.; Wang, M. X.; Gu, L.-Q. Nanopore-Based Detection of Circulating MicroRNAs in Lung Cancer Patients. *Nat. Nanotechnol.* **2011**, *6* (10), 668–674.
- (12) Galenkamp, N. S.; Soskine, M.; Hermans, J.; Wloka, C.; Maglia, G. Direct Electrical Quantification of Glucose and Asparagine From Bodily Fluids Using Nanopores. *Nat. Commun.* **2018**, *9* (1), 4085.
- (13) Thakur, A. K.; Movileanu, L. Single-Molecule Protein Detection in a Biofluid Using a Quantitative Nanopore Sensor. *ACS Sensors* **2019**, *4*, 2320–2326.
- (14) Sze, J. Y. Y.; Ivanov, A. P.; Cass, A. E. G.; Edell, J. B. Single Molecule Multiplexed Nanopore Protein Screening in Human Serum Using Aptamer Modified DNA Carriers. *Nat. Commun.* **2017**, *8* (1), 1552.
- (15) Chen, K.; Zhu, J.; Bošković, F.; Keyser, U. F. Nanopore-Based DNA Hard Drives for Rewritable and Secure Data Storage. *Nano Lett.* **2020**, *20* (5), 3754–3760.
- (16) Cao, C.; Krapp, L. F.; Al Ouahabi, A.; Konig, N. F.; Cirauqui, N.; Radenovic, A.; Lutz, J.-F.; Peraro, M. D. Aerolysin Nanopores Decode Digital Information Stored in Tailored Macromolecular Analytes. *Sci. Adv.* **2020**, *6* (50), 2–10.
- (17) Lopez, R.; Chen, Y.-J.; Dumas Ang, S.; Yekhanin, S.; Makarychev, K.; Racz, M. Z.; Seelig, G.; Strauss, K.; Ceze, L. DNA Assembly for Nanopore Data Storage Readout. *Nat. Commun.* **2019**, *10* (1), 2933.
- (18) Wanunu, M.; Meller, A. Chemically Modified Solid-State Nanopores. *Nano Lett.* **2007**, *7* (6), 1580–1585.
- (19) Spitzberg, J. D.; van Kooten, X. F.; Bercovici, M.; Meller, A. Microfluidic Device for Coupling Isotachophoretic Sample Focusing with Nanopore Single-Molecule Sensing. *Nanoscale* **2020**, *12* (34), 17805–17811.
- (20) Gilboa, T.; Torfstein, C.; Juhasz, M.; Grunwald, A.; Ebenstein, Y.; Weinhold, E.; Meller, A. Single-Molecule DNA Methylation Quantification Using Electro-Optical Sensing in Solid-State Nanopores. *ACS Nano* **2016**, *10* (9), 8861–8870.
- (21) Wang, R.; Gilboa, T.; Song, J.; Huttner, D.; Grinstaff, M. W.; Meller, A. Single-Molecule Discrimination of Labeled DNAs and Polypeptides Using Photoluminescent-Free TiO<sub>2</sub> Nanopores. *ACS Nano* **2018**, *12* (11), 11648–11656.
- (22) Burck, N.; Gilboa, T.; Gadi, A.; Patkin Nehrer, M.; Schneider, R. J.; Meller, A. Nanopore Identification of Single Nucleotide Mutations in Circulating Tumor DNA by Multiplexed Ligation. *Clin. Chem.* **2021**, *67*, 753.
- (23) Li, J.; Stein, D.; McMullan, C.; Branton, D.; Aziz, M. J.; Golovchenko, J. A. Ion-Beam Sculpting at Nanometre Length Scales. *Nature* **2001**, *412* (6843), 166–169.
- (24) Xia, D.; Huynh, C.; McVey, S.; Kobler, A.; Stern, L.; Yuan, Z.; Ling, X. S. Rapid Fabrication of Solid-State Nanopores With High Reproducibility Over a Large Area Using a Helium Ion Microscope. *Nanoscale* **2018**, *10* (11), 5198–5204.
- (25) Storm, A. J.; Chen, J. H.; Ling, X. S.; Zandbergen, H. W.; Dekker, C. Fabrication of Solid-State Nanopores with Single-Nanometre Precision. *Nat. Mater.* **2003**, *2* (8), 537–540.
- (26) Kim, M. J.; Wanunu, M.; Bell, D. C.; Meller, A. Rapid Fabrication of Uniformly Sized Nanopores and Nanopore Arrays for Parallel DNA Analysis. *Adv. Mater.* **2006**, *18* (23), 3149–3153.
- (27) Kwok, H.; Briggs, K.; Tabard-Cossa, V. Nanopore Fabrication by Controlled Dielectric Breakdown. *PLoS One* **2014**, *9* (3), No. e92880.
- (28) Arcadia, C. E.; Reyes, C. C.; Rosenstein, J. K. *In Situ* Nanopore Fabrication and Single-Molecule Sensing with Microscale Liquid Contacts. *ACS Nano* **2017**, *11* (5), 4907–4915.
- (29) Zrehen, A.; Gilboa, T.; Meller, A. Real-Time Visualization and Sub-Diffraction Limit Localization of Nanometre-Scale Pore Formation by Dielectric Breakdown. *Nanoscale* **2017**, *9* (42), 16437–16445.
- (30) Gilboa, T.; Zrehen, A.; Girsault, A.; Meller, A. Optically-Monitored Nanopore Fabrication Using a Focused Laser Beam. *Sci. Rep.* **2018**, *8* (1), 9765.
- (31) Gilboa, T.; Zvuloni, E.; Zrehen, A.; Squires, A. H.; Meller, A. Automated, Ultra-Fast Laser-Drilling of Nanometre Scale Pores and Nanopore Arrays in Aqueous Solutions. *Adv. Funct. Mater.* **2020**, *30*, 1900642.
- (32) Mo, S.-D.; Ching, W. Y. Electronic and Optical Properties of Three Phases of Titanium Dioxide: Rutile, Anatase, and Brookite. *Phys. Rev. B: Condens. Matter Mater. Phys.* **1995**, *51* (19), 13023–13032.
- (33) Madhusudan Reddy, K.; Manorama, S. V.; Ramachandra Reddy, A. Bandgap Studies on Anatase Titanium Dioxide Nanoparticles. *Mater. Chem. Phys.* **2003**, *78* (1), 239–245.
- (34) Yamazaki, H.; Hu, R.; Zhao, Q.; Wanunu, M. Photothermally Assisted Thinning of Silicon Nitride Membranes for Ultrathin Asymmetric Nanopores. *ACS Nano* **2018**, *12* (12), 12472–12481.
- (35) Kim, M. J.; McNally, B.; Murata, K.; Meller, A. Characteristics of Solid-State Nanometre Pores Fabricated Using a Transmission Electron Microscope. *Nanotechnology* **2007**, *18* (20), 205302.
- (36) Bäuerle, D. *Laser Processing and Chemistry*; Springer Science & Business Media: New York, 2013.
- (37) Zrehen, A.; Huttner, D.; Meller, A. On-Chip Stretching, Sorting, and Electro-Optical Nanopore Sensing of Ultralong Human Genomic DNA. *ACS Nano* **2019**, *13* (12), 14388–14398.